

## From Fieldlike Torque to Antidamping Torque in Antiferromagnetic Mn<sub>2</sub>Au

X.F. Zhou,<sup>1</sup> X.Z. Chen,<sup>1</sup> J. Zhang,<sup>2</sup> F. Li,<sup>1</sup> G.Y. Shi,<sup>1</sup> Y.M. Sun,<sup>1</sup> M.S. Saleem,<sup>1</sup> Y.F. You,<sup>1</sup> F. Pan,<sup>1</sup> and C. Song<sup>1,\*</sup>

<sup>1</sup>Key Laboratory of Advanced Materials (MOE), School of Materials Science and Engineering, Tsinghua University, Beijing 100084, China

<sup>2</sup>School of Physics and Wuhan National High Magnetic Field Center, Huazhong University of Science and Technology, Wuhan 430074, China



(Received 21 December 2018; revised manuscript received 13 March 2019; published 10 May 2019)

Efficient electrical switching of antiferromagnets is at the center of their application in high-density and ultrafast nonvolatile memories. Antiferromagnetic (AFM) Mn<sub>2</sub>Au with opposite-spin sublattices is a unique metallic material in which the Edelstein effect can induce fieldlike torque switching of the AFM moments. However, the antidamping-torque-induced AFM moment switching remains to be proved in metallic AFM materials. Here, we demonstrate current-induced AFM moment switching in both a (103)-oriented Mn<sub>2</sub>Au single layer and Mn<sub>2</sub>Au/Pt heterojunction, detected by the spin Hall magnetoresistance and anisotropic magnetoresistance at room temperature. In (103)-oriented Mn<sub>2</sub>Au, fieldlike torque induces the alignment of AFM moments perpendicular to the writing current direction. Once the (103)-oriented Mn<sub>2</sub>Au film is covered by a thin Pt layer, the antidamping torque induced by the spin current from the Pt layer drives the AFM moments of Mn<sub>2</sub>Au switching toward the direction parallel to the writing current, which is in contrast to the case without Pt. The simultaneous realization of fieldlike torque and antidamping torque in metallic Mn<sub>2</sub>Au makes it a promising candidate in AFM spintronics.

DOI: 10.1103/PhysRevApplied.11.054030

### I. INTRODUCTION

Antiferromagnets have potential competitiveness in reliable, high-speed, and high-density information storage for their negligible stray field, strong anti-interference, ultrafast spin dynamics, and ultrafast switching speed [1–5]. Because of their anti-interference nature, it is challenging to manipulate the antiferromagnetic (AFM) moments by magnetic fields, which has stimulated intense interest in and research on manipulating AFM moments [6–13]. Using current-driven spin-transfer torque [14] and spin-orbit torque (SOT) [15,16] is one of the most convenient methods to switch magnetism and favorable progress has been made in ferromagnetic systems, serving as the basis for magnetic random-access memory applications. In antiferromagnets, the current-induced SOT has recently been theoretically predicted [7] and experimentally proved in the fieldlike torque switching of AFM CuMnAs [8,12] and Mn<sub>2</sub>Au with global centrosymmetry plus broken sublattice inversion symmetry [17–19]. The inversion partner sublattices coincide with the two AFM spin sublattices, such that CuMnAs and Mn<sub>2</sub>Au can be switched by a Néel SOT field [7].

Besides this, antidamping torque was also proposed to trigger oscillations and switching of AFM moments [7,20],

[21]. The spin current injecting into the AFM, generated by the spin Hall effect from an adjacent heavy metal (HM) layer, possesses spin polarization with the same sign acting on the two spin sublattices. The local effective fields which are proportional to  $M_{A,B} \times p$  interact on the spin-sublattice magnetizations  $M_{A,B}$  and the antidamping torque  $dM_{A,B}/dt \sim M_{A,B} \times (M_{A,B} \times p)$  on the two spin sublattices is possible to switch the AFM moments. Recently, antidamping-torque-induced magnetic moment switching was observed in a biaxial antiferromagnetic insulator NiO (001)/Pt heterostructure [22]. Obviously there is a pressing need to explore antidamping-torque switching of AFM moments in metals with superior capability for device integration.

Mn<sub>2</sub>Au is selected to demonstrate antidamping-torque-induced switching in this work for two reasons. At first, the comparatively easily prepared metallic antiferromagnet Mn<sub>2</sub>Au exhibits promising potential [23], due to its high Néel temperature above 1000 K [24], huge anisotropic magnetoresistance [17], orientation-dependent switching characteristics [19], and high conductivity. Secondly, compared to other AFM metals, the reported fieldlike torque and possible antidamping torque in Mn<sub>2</sub>Au are combined, providing a unique opportunity to compare them or even use their versatility in spintronics. However, the realization of the antidamping torque in traditional (001)-oriented Mn<sub>2</sub>Au is very challenging because of the large

\* songcheng@mail.tsinghua.edu.cn

out-of-plane magnetocrystalline anisotropy energy (MAE) of meV order [25]. The high index plane is expected to reduce the energy barrier for the spin dynamics process, making the antidamping-torque-induced switching in AFM Mn<sub>2</sub>Au possible. The experiments below demonstrate antidamping torque in (103)-oriented Mn<sub>2</sub>Au covered by a Pt layer, which drives the AFM moment switching toward the direction parallel to the current direction, in contrast to the orthogonal alignment between them for the fieldlike torque in a Mn<sub>2</sub>Au single layer.

## II. METHODS

The 25-nm (103)-oriented Mn<sub>2</sub>Au film is grown on a single-crystal MgO (100) substrate by magnetron sputtering at 573 K from a Mn<sub>2</sub>Au alloy target (atomic ratio of 2:1). The growth rate is 0.07 nm/s and the base pressure is  $2.5 \times 10^{-5}$  Pa. The high-resolution transmission electron microscopy (HRTEM) of (103)-oriented Mn<sub>2</sub>Au film is carried out on a JEM 2100 manufactured by JEOL. The roughness of film is measured by an atomic force microscope. The magnetic properties are measured by superconducting quantum interference device (SQUID) magnetometry. The eight-terminal devices for our SOT switching are fabricated by photolithography and argon ion milling procedures. The writing current pulses are generated by a Keysight B2961A source meter. After each writing pulse, a 10-s delay is used for thermal relaxation. A reading current generated by an Agilent B2901A source meter is applied across the central area, while the transversal Hall voltage is recorded to read the Hall resistance. The MAE of (103)-oriented Mn<sub>2</sub>Au is calculated by using standard force theory (FT). According to the symmetry of the bulk Mn<sub>2</sub>Au, the MAE can be expressed by  $E(\theta, \varphi) = K_{2\perp} \sin^2 \theta + K_{4\perp} \sin^4 \theta + K_{4//} / \sin^4 \theta \cos 4\varphi$  [19,25]. Here,  $\theta$  and  $\varphi$  are the angles between magnetization ( $\mathbf{M}$ ) and the [001] axis and the angle between the projection direction of  $\mathbf{M}$  on the Mn<sub>2</sub>Au (001) plane and [100] axis, respectively;  $K_{2\perp}$ ,  $K_{4\perp}$ , and  $K_{4//}$  parameterize the uniaxial MAE constant, the fourth-order out-of-plane MAE constant, and fourth-order in-plane MAE constant, respectively. The lattice constants of Mn<sub>2</sub>Au used in the first-principles calculations are obtained by x-ray diffraction (XRD) experiments. Through first-principles calculations, the MAE constants  $K_{2\perp}$ ,  $K_{4\perp}$ , and  $K_{4//}$  can be obtained according to the lattice constant (see Table S1 of Ref. [26] for the MAE constants). The atomic position is fully relaxed. A self-consistency of electron charge density is performed without spin-orbit coupling. Then, a one-step calculation is done with the consideration of spin-orbit coupling when the magnetization is aligned along different axes and the MAE is evaluated by a band energy difference.

## III. RESULTS

Figure 1(a) shows XRD spectra of 25-nm-thick Mn<sub>2</sub>Au films grown by magnetron sputtering on a MgO (100) substrate, where the diffraction peaks from (103) planes can be clearly seen, indicating the quasiepitaxial growth of (103)-oriented Mn<sub>2</sub>Au films (see Fig. S1 of Ref. [26] for details of the pole figure). All films are Mn<sub>2</sub>Au single phase with no evidence of secondary phases within the sensitivity of XRD measurements. A typical cross-sectional resolution transmission electron microscopy (HRTEM) image of the MgO (100) substrate-Mn<sub>2</sub>Au (103) films is presented in Fig. 1(b). There is no grain boundary in the overall films, confirming the quasiepitaxial growth mode of the Mn<sub>2</sub>Au films. Such a quasiepitaxial growth mode guarantees a small surface roughness of 0.134 nm measured by atomic force microscope (see Fig. S2 of Ref. [26] for details of the atomic force microscope image). This feature serves as the basis for the deposition of a continuous Pt layer on the Mn<sub>2</sub>Au films, which is discussed below.

SQUID magnetometry is used to measure the magnetic properties of the Mn<sub>2</sub>Au films. The magnetic field is applied in plane, i.e., parallel to the (001) plane and [100] edge of the MgO substrate. The representative magnetization curve of the Mn<sub>2</sub>Au (103) film at 300 K is displayed in Fig. 1(c). We can observe typical diamagnetic signals up to 50 kOe, which reflects the diamagnetic feature of the MgO substrate. Hence, the Mn<sub>2</sub>Au is an antiferromagnetic film without any ferromagnetic signal.

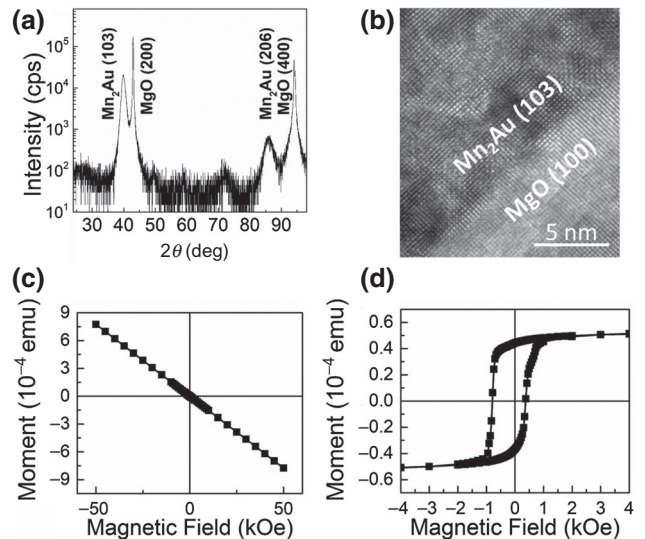


FIG. 1. Characterization and analysis of quasiepitaxial Mn<sub>2</sub>Au (103) films. (a) XRD spectra. (b) HRTEM image of the MgO (100) substrate/Mn<sub>2</sub>Au (103) cross section. (c) Room temperature magnetization curve of the Mn<sub>2</sub>Au (103) film deposited on the MgO (100) substrate. (d) Magnetic hysteresis loop of Mn<sub>2</sub>Au (10 nm)/NiFe (5 nm) bilayers grown on the MgO (100) substrate, after 10 kOe field cooling from 300 to 20 K.

Moreover, in order to further confirm the antiferromagnetism of Mn<sub>2</sub>Au, 5-nm-thick permalloy is deposited on top of 10-nm Mn<sub>2</sub>Au. The corresponding magnetization curve of Mn<sub>2</sub>Au (10 nm)/NiFe (5 nm) at 20 K, after 10 kOe field cooling from 300 K, is depicted in Fig. 1(d). The hysteresis loop exhibits an apparent shift of 200 Oe compared to its coercivity of 580 Oe; the exchange bias phenomenon reaffirms the antiferromagnetism of the Mn<sub>2</sub>Au film.

The MAE of (103)-oriented Mn<sub>2</sub>Au is calculated by using standard force theory to find the easy axes of Mn<sub>2</sub>Au, so that the magnetic moments of Mn<sub>2</sub>Au can be switched by current between two easy axes. As calculated in the previous work [25], the (001) plane is the lowest energy plane (easily magnetized plane) of Mn<sub>2</sub>Au. Figure 2(a) illustrates the calculated in-plane angular  $\varphi$  dependence of MAE. The

lowest energy appears at  $\varphi$  values of 90° and 180°, indicating that the in-plane easy axes are along [100] and [010]. It is different from the [110] and [1̄10] easy axes of (001)-oriented Mn<sub>2</sub>Au [17,25,27,28], but it is reasonable. The MAE difference for an easily magnetized plane is small, and the (103)-oriented Mn<sub>2</sub>Au film grows on the MgO substrate, while the (001)-oriented Mn<sub>2</sub>Au film grows on the Al<sub>2</sub>O<sub>3</sub> substrate, which produces different strain and induces different MAE. The MAE distribution provides the potential ability that the magnetic moments of (103)-oriented Mn<sub>2</sub>Au can be switched by current between two easy axes [100] and [010].

Figure 2(b) depicts a schematic of the eight-terminal device, in which the measurement configuration is included and the channel width is 5  $\mu\text{m}$ . The experiment

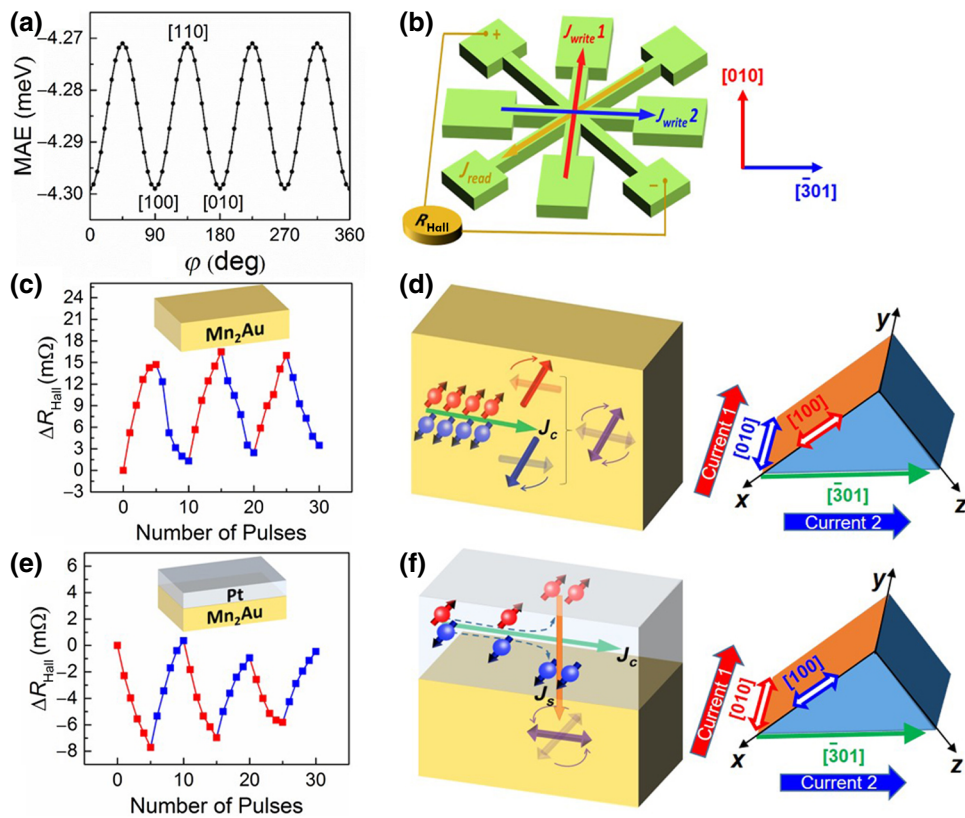


FIG. 2. Calculated MAE curves as well as a comparison of the SOT switching measurements in eight-terminal devices based on a (103)-oriented Mn<sub>2</sub>Au single layer and Mn<sub>2</sub>Au/Pt bilayers. (a) Calculated MAE curves of Mn<sub>2</sub>Au (103) film deposited on a MgO (100) substrate. (b) Schematic of the eight-terminal device and the switching measurement geometry. Writing current pulses are applied along the red ( $J_{\text{write}1}$ ) and blue arrows ( $J_{\text{write}2}$ ) alternatively, corresponding to two orthogonal directions, [010] and [301], of Mn<sub>2</sub>Au (103) films. Reading current is marked as the orange arrow and the Hall resistance is detected in its transverse direction simultaneously. (c) The Hall resistance changes as a function of the number of writing current pulses in 10-nm (103)-orientated Mn<sub>2</sub>Au. The variation of Hall resistance is shown as red and blue squares for the writing current pulse along [010] and [301], respectively. (d) Schematic of fieldlike torque-induced Néel order switching of a Mn<sub>2</sub>Au single layer. The relationship between current directions and the easy axes after writing current are shown in the right panel. Hollow double arrows represent the antiferromagnetic easy axes and solid thick arrows denote the current directions. The gold plane marks (001) plane and green arrow represents [301], the projection of a [100] axis in the (103) plane. (e) Hall resistance changes as a function of the number of writing current pulses in Mn<sub>2</sub>Au (103) (10 nm)/Pt (7 nm) bilayers. (f) Schematic of the antidamping torque-induced Néel order switching in Mn<sub>2</sub>Au/Pt bilayers. The relationship between current directions and the easy axes after writing currents is shown in the right panel.

is performed in the following way: five successive 1-ms-duration writing current pulses of  $J_{\text{write}}$  are applied along the [010] axis (red arrow,  $J_{\text{write}1}$ ) and then along the orthogonal direction of [010] axis, the [301] axis (blue arrow,  $J_{\text{write}2}$ ), which is the projection of the easy axis [100] direction in the (103) plane of Mn<sub>2</sub>Au. As indicated above, this plane is parallel to the substrate surface. The Hall resistance ( $R_{\text{Hall}}$ ) is recorded to detect the switching of Mn<sub>2</sub>Au magnetic moments. The five current pulses along the [010] axis ( $J_{\text{write}1}$ ) switch the AFM moments to the [100] axis (perpendicular to the [010] axis), which gradually increases the Hall resistance. Then, the same five pulses along the [301] axis ( $J_{\text{write}2}$ ) drive the AFM moments rotating back to the [010] direction, and thus the Hall resistance decreases in the opposite sign. After that, five current pulses along the [010] axis increase the Hall resistance again. Such a switching experiment is conducted in three circles. Corresponding data are presented in Fig. 2(c), where the Hall resistance variation ( $\Delta R_{\text{Hall}}$ ) is shown as a function of the number of current pulses in a device made from 10-nm (103)-oriented Mn<sub>2</sub>Au and five successive current pulses along the [010] and [301] axes alternatively. A threshold writing current density of  $1.4 \times 10^8 \text{ A cm}^{-2}$  (70 mA) is needed to drive fieldlike torque in the Mn<sub>2</sub>Au single layer. As expected, this switching feature reflects that the fieldlike torque switch the AFM moments perpendicular to the writing current direction [7,8,17]. This result is caused by the inverse spin galvanic effects and resultantly opposite effective magnetic field at the sublattices, as illustrated in Fig. 2(d) [7]. Also visible is that the gradually enhanced Hall resistance reflects the multidomain switching feature of the present Néel SOT. The continuously varied Hall resistance has promising uses in neuromorphic computing.

The situation turns out to be dramatically different when a Pt layer is deposited on the Mn<sub>2</sub>Au films. Figure 2(e) presents the current-pulse-dependent  $\Delta R_{\text{Hall}}$  for the 10-nm Mn<sub>2</sub>Au (103) covered by 7 nm of Pt. The device configuration and measurement scheme are identical to those in the scenario of Fig. 2(b) (without Pt). Nevertheless, the tendency of the Hall resistance variation goes opposite to the case without Pt. In this case,  $J_{\text{write}1}$  and  $J_{\text{write}2}$  reduce and enhance Hall resistance, respectively. The variation tendency suggests that the AFM moments tend to be parallel to the writing current direction in the Mn<sub>2</sub>Au/Pt sample. The threshold writing current density in the bilayers is calculated to be approximately  $7.1 \times 10^7 \text{ A cm}^{-2}$ , taking the critical current of 60 mA for the AFM switching. The current is greatly shunted to the 7-nm-thick Pt from the 10-nm-thick Mn<sub>2</sub>Au in the bilayers sample, due to much lower resistivity of the Pt layer compared to Mn<sub>2</sub>Au,  $3.1 \times 10^{-7} \Omega \text{ m}$  and  $9.6 \times 10^{-7} \Omega \text{ m}$ , respectively, which is obtained by the four probe measurements. Hence, the fieldlike torque in the Mn<sub>2</sub>Au bulk film is overshadowed by the antidamping torque in the Mn<sub>2</sub>Au/Pt bilayers. The

antidamping torque-induced switching mechanism can be explained as follows [Fig. 2(f)]: the strong current in the heavy metal Pt generates spin current with the same spin polarization flowing into the Mn<sub>2</sub>Au layer, producing the antidamping torque. The antidamping-torque-induced switching in biaxial antiferromagnets can be described by a two-step process: it firstly deviates from one easy axis and is confined in the plane perpendicular to the spin polarization, and secondly, it switches toward another easy axis contained in the same plane, resulting in the parallel configuration between the current and Néel order [22].

We then turn toward the Pt top layer thickness-dependent SOT switching in Mn<sub>2</sub>Au (25 nm)/Pt ( $t = 0, 1, 3$ , and 7 nm) samples. Concomitant data are displayed in Figs. 3(a)–3(d).  $\Delta R_{\text{Hall}}$  as a function of current pulse numbers for the 25-nm-thick Mn<sub>2</sub>Au film in Fig. 3(a) shows a qualitatively similar feature as the 10-nm one in Fig. 2(c), reflecting the current-driven fieldlike torque in the Mn<sub>2</sub>Au single layer with different film thicknesses. The growth of 1 nm of Pt on top of the 25-nm Mn<sub>2</sub>Au cannot change the switching characters, as shown in Fig. 3(b). The 1-nm-thick Pt layer behaves as a continuous film on the rather smooth Mn<sub>2</sub>Au (see Fig. S3 of Ref. [26] for details of the atomic force microscope image), similar to the uniform 1-nm-thick Pt on Y<sub>3</sub>Fe<sub>5</sub>O<sub>12</sub> films [29]. Although the Pt layer is continuous and can be conductive, the ultrathin Pt (e.g., 1 nm) does not shunt enough current for the sizable spin current and resultant antidamping torque, which

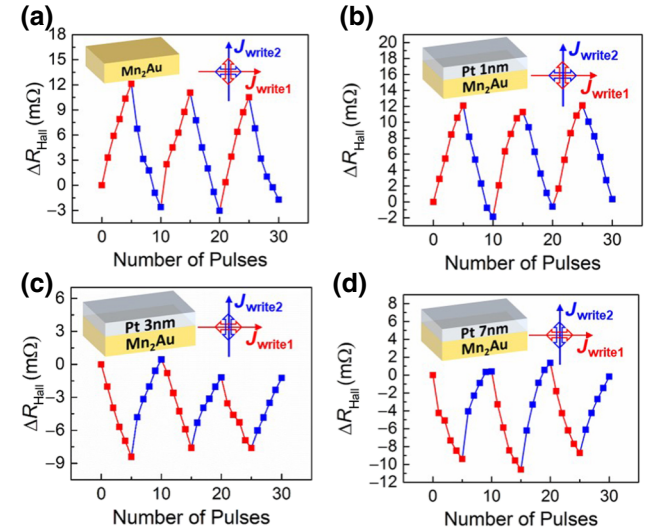


FIG. 3. Variation of Hall resistance in different platinum thickness samples: (a) Mn<sub>2</sub>Au (25 nm), (b) Mn<sub>2</sub>Au (25 nm)/Pt (1 nm), (c) Mn<sub>2</sub>Au (25 nm)/Pt (3 nm), (d) Mn<sub>2</sub>Au (25 nm)/Pt (7 nm). The heterostructure is shown in the left insets. The relationship between the current direction (solid arrows, red for  $J_{\text{write}1}$  and blue for  $J_{\text{write}2}$ ) and corresponding AFM moment direction (hollow arrows) after each current schematic is shown in the right insets.

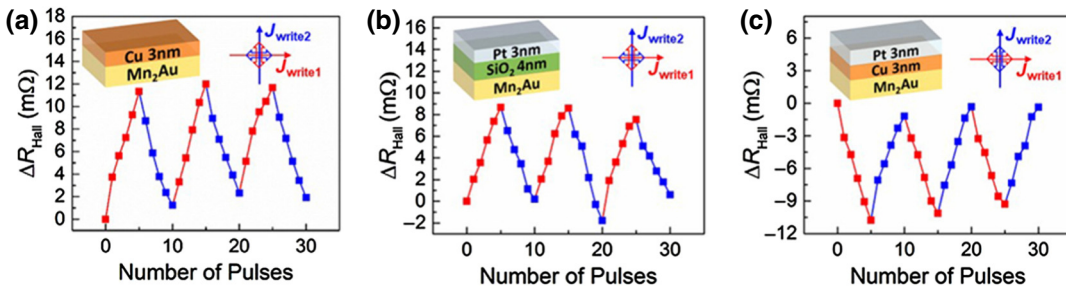


FIG. 4. Variation of Hall resistance in different control samples: (a) Mn<sub>2</sub>Au (25 nm)/Cu (3 nm), (b) Mn<sub>2</sub>Au (25 nm)/SiO<sub>2</sub> (4 nm)/Pt (3 nm), (c) Mn<sub>2</sub>Au (25 nm)/Cu (3 nm)/Pt (3 nm). The heterostructure is shown in the left insets. The relationship between the current direction (solid arrows, red for  $J_{\text{write}1}$  and blue for  $J_{\text{write}2}$ ) and corresponding AFM moment direction (hollow arrows) after each current schematic is shown in the right insets.

is completely overshadowed by the fieldlike torque in the Mn<sub>2</sub>Au itself. The orthogonal arrangement between the current and Néel order remains.

Interestingly, when the Pt layer thickness increases to 3 nm, the Hall resistance of the Mn<sub>2</sub>Au (25 nm)/Pt (3 nm) sample initially decreases with  $J_{\text{write}1}$  and then increases with  $J_{\text{write}2}$ , as illustrated in Fig. 3(c), analogous to the scenario of the Mn<sub>2</sub>Au (10 nm)/Pt (7 nm) bilayers shown in Fig. 2(e). This switching undergoes an opposite tendency to the scenario of the Mn<sub>2</sub>Au single layer and Mn<sub>2</sub>Au (25 nm)/Pt (1 nm) sample. When increasing the Pt thickness to 7 nm, the switching feature remains qualitatively the same. It is demonstrated that the antidamping torque emerges once the Pt is up to a certain thickness of 3 nm, revealing the generation of spin current by the spin Hall effect in the bulk Pt films. The critical currents for the AFM switching of Mn<sub>2</sub>Au (25 nm)/Pt ( $t = 0, 1, 3$ , and 7 nm) are  $5.44 \times 10^7$ ,  $5.38 \times 10^7$ ,  $4.28 \times 10^7$ , and  $3.75 \times 10^7$  A cm<sup>-2</sup>, respectively. Hence, when the Mn<sub>2</sub>Au is covered by 3 nm of Pt, the antidamping torque switches Mn<sub>2</sub>Au moments rather than the fieldlike torque, because the writing current is not up to the threshold current density of the fieldlike torque of the Mn<sub>2</sub>Au. Moreover, the longitudinal resistance variations are measured (see Fig. S4 of Ref. [26] for details of longitudinal geometries), which is in agreement with the variation direction of the Hall resistance that the antiferromagnetic moments are switched perpendicular to writing current in Mn<sub>2</sub>Au (25 nm) and parallel in Mn<sub>2</sub>Au (25 nm)/Pt (3 nm).

An identical device configuration and measurement setup are used for the 25-nm Mn<sub>2</sub>Au sample covered by a 3-nm-thick Cu layer [Fig. 4(a)]. Remarkably, the existence of the Cu cap has a negligible effect on the switching character and the fieldlike torque switching feature of Mn<sub>2</sub>Au remains, which demonstrates the important role of heavy metal Pt on the antidamping torque. In addition, to disclose the key role of the spin current produced by the Pt layer on the antidamping torque, 4-nm-thick SiO<sub>2</sub> is inserted between the 25-nm Mn<sub>2</sub>Au and 3-nm Pt to block the spin current from Pt to Mn<sub>2</sub>Au [Fig. 4(b)]. The switching

feature remains the same as the Mn<sub>2</sub>Au single layer, indicating that the fieldlike torque remains. Considering that the proximity effect may be introduced at the Mn<sub>2</sub>Au/Pt interface, 3-nm-thick Cu is inserted between the 25-nm Mn<sub>2</sub>Au and 3-nm Pt that can pass spin current and blocks the proximity effect at the Mn<sub>2</sub>Au/Pt interface [Fig. 4(c)]. The same switching feature as Mn<sub>2</sub>Au/Pt bilayers reveals that the antidamping torque switching is mainly caused by the spin current generated in the heavy metal Pt, rather than the interfacial Rashba effect, Dzyaloshinsky-Moriya interaction, and Pt proximity effect, which possibly exists at the Mn<sub>2</sub>Au/Pt interface. It is then concluded that the reversal of the switching behaviors indeed arises from the spin current generated by the spin Hall effect in Pt.

#### IV. DISCUSSION

We then address the question why the antidamping-torque-induced switching could be observed in the present Mn<sub>2</sub>Au (103)/Pt bilayers. For the antidamping torque in the AFM system, the Néel order  $l$  starts the precession around the spin polarization  $p$  and then evolves toward the plane perpendicular to the spin polarization,  $l \perp p$ . In this case, the out-of-plane direction is involved in the Néel order precession, which possesses a comparatively large out-of-plane magnetic anisotropy energy at the order of meV, challenging the antidamping torque in (001)-oriented films [25]. However, when the current is applied along the [010] direction of Mn<sub>2</sub>Au (103), the Néel order precession occurs in the plane perpendicular to the spin polarization direction [301]. The tilting angle from the (001) plane to the (103) plane makes the Néel order precession comparatively easier and then allows the antidamping-torque-induced AFM switching between two easy axes in the Mn<sub>2</sub>Au (103) films. As for the detection of AFM moment switching, it should be addressed that in our Mn<sub>2</sub>Au/Pt system, both the SMR [30–32] and AMR [8] can contribute to the resistance variation. The SMR has its minimum value for the Néel vector aligned perpendicular to the probing current direction [22,30]. The AMR also has

its minimum value for the Néel vector aligned perpendicular to the probing current direction, which has been proved in FeRh [33] and CuMnAs [8] at room temperature. Similar results of Mn<sub>2</sub>Au are shown in Fig. S4. Hence, the SMR has the same change tendency as the AMR of Mn<sub>2</sub>Au, so that both SMR and AMR contribute to the variation of Hall and longitudinal resistances.

## V. CONCLUSION

In summary, we demonstrate current-induced AFM moment switching in both a (103)-oriented Mn<sub>2</sub>Au single layer and Mn<sub>2</sub>Au/Pt heterojunction, which are detected by the SMR and AMR at room temperature. The switching mechanisms for the Mn<sub>2</sub>Au single layer and Mn<sub>2</sub>Au/Pt bilayers (Pt film thickness  $\geq 3\text{ nm}$ ) are fieldlike torque and antidamping torque, leading to the AFM moments of Mn<sub>2</sub>Au toward the direction perpendicular and parallel to the writing current, respectively. The simultaneous realization of fieldlike torque and antidamping torque in metallic Mn<sub>2</sub>Au ensures its versatility in AFM spintronics.

## ACKNOWLEDGMENTS

C.S. acknowledges the support of the Beijing Innovation Center for Future Chip (ICFC) and Young Chang Jiang Scholars Program. This work is supported by the National Natural Science Foundation of China (Grant No. 51871130), the National Key R&D Program of China (Grant No. 2017YFB0405704), and the National Natural Science Foundation of China (Grants No. 51571128 and No. 51671110).

- [1] T. Jungwirth, X. Martí, P. Wadley, and J. Wunderlich, Antiferromagnetic spintronics, *Nat. Nanotechnol.* **11**, 231 (2016).
- [2] J. Železný, P. Wadley, K. Olejník, A. Hoffmann, and H. Ohno, Spin transport and spin torque in antiferromagnetic devices, *Nat. Phys.* **14**, 220 (2018).
- [3] V. Baltz, A. Manchon, M. Tsoi, T. Moriyama, T. Ono, and Y. Tserkovnyak, Antiferromagnetic spintronics, *Rev. Mod. Phys.* **90**, 015005 (2018).
- [4] W. Zhang and K. M. Krishnan, Epitaxial exchange-bias systems: From fundamentals to future spin-orbitronics, *Mater. Sci. Eng. R* **105**, 1 (2016).
- [5] C. Song, Y. F. You, X. Z. Chen, X. F. Zhou, Y. Y. Wang, and F. Pan, How to manipulate magnetic states of antiferromagnets, *Nanotechnology* **29**, 112001 (2018).
- [6] B. G. Park, J. Wunderlich, X. Martí, V. Holý, Y. Kuroasaki, M. Yamada, H. Yamamoto, A. Nishide, J. Hayakawa, H. Takahashi, A. B. Shick, and T. Jungwirth, A spin-valve-like magnetoresistance of an antiferromagnet-based tunnel junction, *Nat. Mater.* **10**, 347 (2011).
- [7] J. Železný, H. Gao, K. Výborný, J. Zemen, J. Mašek, Aurélien Manchon, J. Wunderlich, Jairo Sinova, and T.

Jungwirth, Relativistic Néel-Order Fields Induced by Electrical Current in Antiferromagnets, *Phys. Rev. Lett.* **113**, 157201 (2014).

- [8] P. Wadley, *et al.*, Electrical switching of an antiferromagnet, *Science* **351**, 587 (2016).
- [9] Y. Y. Wang, C. Song, B. Cui, G. Y. Wang, F. Zeng, and F. Pan, Room-Temperature Perpendicular Exchange Coupling and Tunneling Anisotropic Magnetoresistance in Antiferromagnet-Based Tunnel Junction, *Phys. Rev. Lett.* **109**, 137201 (2012).
- [10] X. Z. Chen, J. F. Feng, Z. C. Wang, J. Zhang, X. Y. Zhong, C. Song, L. Jin, B. Zhang, F. Li, M. Jiang, Y. Z. Tan, X. J. Zhou, G. Y. Shi, X. F. Zhou, X. D. Han, S. C. Mao, Y. H. Chen, X. F. Han, and F. Pan, Tunneling anisotropic magnetoresistance driven by magnetic phase transition, *Nat. Commun.* **8**, 449 (2017).
- [11] C. Song, B. Cui, F. Li, X. Zhou, and F. Pan, Recent progress in voltage control of magnetism: Materials, mechanisms, and performance, *Prog. Mater. Sci.* **87**, 33 (2017).
- [12] M. J. Grzybowski, P. Wadley, K. W. Edmonds, R. Beardsley, V. Hills, R. P. Campion, B. L. Gallagher, J. S. Chauhan, V. Novak, T. Jungwirth, F. Maccherozzi, and S. S. Dhesi, Imaging Current-Induced Switching of Antiferromagnetic Domains in CuMnAs, *Phys. Rev. Lett.* **118**, 057701 (2017).
- [13] T. Moriyama, K. Oda1, T. Ohkochi, M. Kimata, and T. Ono, Spin torque control of antiferromagnetic moments in NiO, *Sci. Rep.* **8**, 14167 (2018).
- [14] D. C. Ralph and M. D. Stiles, Spin transfer torques, *J. Magn. Magn. Mater.* **320**, 1190 (2008).
- [15] L. Liu, C. F. Pai, Y. Li, H. W. Tseng, D. C. Ralph, and R. A. Buhrman, Spin-torque switching with the giant spin Hall effect of tantalum, *Science* **336**, 555 (2012).
- [16] Y. B. Fan, P. Upadhyaya, X. F. Kou, M. R. Lang, S. Takei, Z. Wang, J. S. Tang, L. He, L. T. Chang, M. Montazeri, and K. L. Wang, Magnetization switching through giant spin-orbit torque in a magnetically doped topological insulator heterostructure, *Nat. Mater.* **13**, 699 (2014).
- [17] S. Yu. Bodnar, L. Šmejkal, I. Turek, T. Jungwirth, O. Gomonay, J. Sinova, A. A. Sapozhnik, H. J. Elmers, M. Kläui, and M. Jourdan, Writing and reading antiferromagnetic Mn<sub>2</sub>Au: Néel spin-orbit torques and large anisotropic magnetoresistance, *Nat. Commun.* **9**, 348 (2018).
- [18] M. Meinert, D. Graulich, and T. Matalla-Wagner, Electrical Switching of antiferromagnetic Mn<sub>2</sub>Au and the role of thermal activation, *Phys. Rev. Appl.* **9**, 064040 (2018).
- [19] X. F. Zhou, J. Zhang, F. Li, X. Z. Chen, G. Y. Shi, Y. Z. Tan, Y. D. Gu, M. S. Saleem, H. Q. Wu, F. Pan, and C. Song, Strong orientation dependent spin-orbit torque in antiferromagnet Mn<sub>2</sub>Au, *Phys. Rev. Appl.* **9**, 054028 (2018).
- [20] R. Zarzuela and Y. Tserkovnyak, Antiferromagnetic textures and dynamics on the surface of a heavy metal, *Phys. Rev. B* **95**, 180402(R) (2017).
- [21] H. V. Gomonay and V. M. Loktev, Spin transfer and current-induced switching in antiferromagnets, *Phys. Rev. B* **81**, 144427 (2010).
- [22] X. Z. Chen, R. Zarzuela, J. Zhang, C. Song, X. F. Zhou, G. Y. Shi, F. Li, H. A. Zhou, W. J. Jiang, F. Pan, and Y. Tserkovnyak, Antidamping-Torque-Induced Switching in Biaxial Antiferromagnetic Insulators, *Phys. Rev. Lett.* **120**, 207204 (2018).

- [23] H. C. Wu, Z. M. Liao, R. G. Sumesh Sofin, G. Feng, X. M. Ma, A. B. Shick, O. N. Mryasov, and I. V. Shvets, Mn<sub>2</sub>Au: Body-centered-tetragonal bimetallic antiferromagnets grown by molecular beam epitaxy, *Adv. Mater.* **24**, 6374 (2012).
- [24] V. M. T. S. Barthem, C. V. Colin, H. Mayaffre, M. H. Julien, and D. Givord, Revealing the properties of Mn<sub>2</sub>Au for antiferromagnetic spintronics, *Nat. Commun.* **4**, 2892 (2013).
- [25] A. B. Shick, S. Khmelevskyi, O. N. Mryasov, J. Wunderlich, and T. Jungwirth, Spin-orbit coupling induced anisotropy effects in bimetallic antiferromagnets: A route towards antiferromagnetic spintronics, *Phys. Rev. B* **81**, 212409 (2010).
- [26] See Supplemental Material at <http://link.aps.org-supplemental/10.1103/PhysRevApplied.11.054030> for MAE parameters, pole figure, and atomic force microscope images.
- [27] V. M. T. S. Barthem, C. V. Colin, R. Haettel, D. Dufeu, and D. Givord, Easy moment direction and antiferromagnetic domain wall motion in Mn<sub>2</sub>Au, *J. Magn. Magn. Mater.* **406**, 289 (2015).
- [28] A. A. Sapozhnik, M. Filianina, S. Yu. Bodnar, A. Lamirand, M. A. Mawass, Y. Skourski, H. J. Elmers, H. Zabel, M. Kläui, and M. Jourdan, Direct imaging of antiferromagnetic domains in Mn<sub>2</sub>Au manipulated by high magnetic fields, *Phys. Rev. B* **97**, 134429 (2018).
- [29] L. F. Zhou, H. K. Song, K. Liu, Z. Z. Luan, P. Wang, L. Sun, S. W. Jiang, H. J. Xiang, Y. B. Chen, J. Du, H. F. Ding, K. Xia, J. Xiao, and D. Wu, Observation of spin-orbit magnetoresistance in metallic thin films on magnetic insulators, *Sci. Adv.* **4**, eaao3318 (2018).
- [30] H. Wang, D. Z. Hou, Z. Y. Qiu, T. Kikkawa, E. Saitoh, and X. F. Jin, Antiferromagnetic anisotropy determination by spin Hall magnetoresistance, *J. Appl. Phys.* **122**, 083907 (2017).
- [31] D. Z. Hou, Z. Y. Qiu, J. Barker, K. J. Sato, K. Yamamoto, S. Vélez, J. M. Gomez-Perez, L. E. Hueso, F. Casanova, and E. Saitoh, Tunable Sign Change of Spin Hall Magnetoresistance in Pt/NiO/YIG Structures, *Phys. Rev. Lett.* **118**, 147202 (2017).
- [32] L. Baldrati, A. Ross, T. Niizeki, C. Schneider, R. Ramos, J. Cramer, O. Gomonay, M. Filianina, T. Savchenko, D. Heinze, A. Kleibert, E. Saitoh, J. Sinova, and M. Kläui, Full angular dependence of the spin Hall and ordinary magnetoresistance in epitaxial antiferromagnetic NiO(001)/Pt thin films, *Phys. Rev. B* **98**, 024422 (2018).
- [33] X. Marti, *et al.*, Room-temperature antiferromagnetic memory resistor, *Nat. Mater.* **13**, 367 (2014).